Lithosphere

Research Article

Multiscale Sensitivity Analysis of Hydraulic Fracturing Parameters Based on Dimensionless Analysis Method

Haoran Luo,[1] Jun Xie,[2] Liuke Huang [ID],[3,4,5] Jianfa Wu,[1] Xuewen Shi,[1] Yuesong Bai,[6,7] Haifeng Fu,[8] and Bing Pan[9]

[1]*Shale Gas Research Institute, PetroChina Southwest Oil & Gas Field Company, Chengdu, Sichuan 610051, China*
[2]*China National Petroleum Corporation, Beijing 100007, China*
[3]*Department of Geotechnical Engineering, College of Civil Engineering, Tongji University, Shanghai 200092, China*
[4]*School of Civil Engineering and Geomatics, Southwest Petroleum University, Chengdu, Sichuan 610500, China*
[5]*State Key Laboratory of Geomechanics and Geotechnical Engineering, Institute of Rock and Soil Mechanics, Chinese Academy of Sciences, Wuhan 430071, China*
[6]*Institute of Mining Technology, Taiyuan University of Technology, Taiyuan 030024, China*
[7]*Shanxi Wangjialing Coal Industry Co. Ltd., Xinzhou 036600, China*
[8]*Research Institute of Petroleum Exploration and Development, PetroChina, Langfang 065007, China*
[9]*HydroChina ITASCA R and D Center, Hangzhou 311122, China*

Correspondence should be addressed to Liuke Huang; swpuhlk@126.com

The optimal design of hydraulic fracturing parameters is the key to commercial exploitation of unconventional reservoirs. Hydraulic fracturing test is one of the main methods for optimizing fracturing parameters. It is known that scale effect exists between laboratory experiments and field treatments of hydraulic fracturing. However, studies on how to eliminate the scale effect are rarely reported. In this work, we conduct sensitivity analysis on rock mechanical parameters and fracturing parameters at different scales by using the dimensionless analysis method. The initiation and propagation process of field hydraulic fracturing is reproduced through laboratory tests, and fracturing parameters are analyzed by using numerical simulation. Our results show that the fracture propagation in the laboratory is inconsistent with that in the field fracturing. The fracture initiation and propagation in the field can be reproduced in experiments by using samples with high modulus and low toughness as well as high-viscosity fracturing fluid. Microcracks are created before the breakdown pressure is reached, and hydraulic fractures extend perpendicular to the direction of the minimum principal stress. The Carter's leak-off coefficient has little effect on breakdown pressure and propagation pressure, but the injection rate and the horizontal principal stress have significant effects on breakdown pressure. This study provides a theoretical basis and guidance for the design of fracturing parameters both in the laboratory and in the field.

1. Introduction

The optimal design of hydraulic fracturing parameters is the key to commercial exploitation of unconventional reservoirs [1–4]. Therefore, it is important to clarify the influence mechanism of rock mechanical parameters and fracturing operational parameters on fracture propagation during hydraulic fracturing. The dynamic propagation behavior of hydraulic fractures is influenced by mechanical properties of the reservoir, fracturing fluid parameters, and fracturing operations.

Among these factors, rock modulus, fracture toughness, injection rate, fracturing fluid viscosity, and fracturing time are important parameters that determine fracture length and fracture aperture [5–11]. It is also important to determine the fracture initiation pressure and propagating pressure.

Hydraulic fracturing is a complex process that involves multifield and multiscale coupling [12–14]. It involves fracture initiation and propagation in the near wellbore region [15], and in the far field, multiple hydraulic fractures interfere with each other [16, 17]. In other words, the time scale, spatial

scale, and main control factors involved in each hydraulic fracturing process are different. These factors can cause hydraulic fractures to propagate in any direction and form complex fracture networks. When hydraulic fractures propagate in the near wellbore region, patterns such as turning fractures, T-shaped fractures, and multiple parallel fractures can occur with asymmetric and nonplanar propagation and competition between perforations [11, 18–21]. Multistage fracturing has been widely used in the field [22]. Competitive propagation and fracture diversion can occur during hydraulic fracturing due to stress shadow effects [23]. In addition, because of the lack of accurate characterization of reservoir properties and effective simulation of complex fracture networks, the actual fracturing process still heavily depends on experience [24, 25]. Therefore, the accurate prediction of hydraulic fracture geometry remains an unsolved problem.

Fracturing design is the basis for fracturing operations, which has an important impact on oil and gas production. Researchers have studied hydraulic fracturing through theoretical analyses, laboratory experiments, and numerical simulations [13, 22, 23, 26–33]. The classical KGD model, PKN model, and radial model are mainly used for fast calculation of hydraulic fracture geometries in theoretical analysis [34, 35]. Furthermore, scholars have established quasi three-dimensional (3D) models, planar 3D models, and full 3D models [31, 36–39]. In the past decade, remarkable progress has been made in the numerical simulation of hydraulic fracturing with the rapid development of unconventional resources. These numerical methods can be divided into several categories depending on the theoretical context. From the perspective of continuum mechanics, finite element methods include the cohesive method, the extended finite element method, and the boundary element method [3, 11, 22, 30, 40, 41]. From the perspective of discretization, numerical methods include the block discrete element method, the particle discrete element method, and the 3D lattice method [10, 15, 42, 43]. In addition, some new numerical methods are also used to model hydraulic fracturing, such as the material point method, the peridynamics method, the finite-discrete element method, and the phase field method [44–47].

The current numerical simulations, however, are mainly aimed at two-dimensional (2D) and quasi 3D approximate simulations, and limited studies exist on complex 3D nonplanar fracture propagation [3, 33, 48, 49]. In addition, current theoretical analyses cannot describe the complex nonplanar propagation process of multiple hydraulic fractures. For monitoring technology, it is difficult to monitor the complex propagation process of fractures and accurately evaluate the fracturing effect. As a result, hydraulic fracturing testing in the laboratory has become a useful method [50]. Compared with fracturing parameters in the field, some parameters in the laboratory tests are very small. Therefore, scale effects exist between laboratory experiments and field treatments of hydraulic fracturing. For example, the length of hydraulic fracture in the experiment is normally less than 1 m, while the field scale is in the order of kilometer [51, 52]. The injection rate in the laboratory tests is generally in the order of ml/min, while the field injection rate can reach 18 m³/min.

Studies on how to eliminate scale effects are rarely reported. To this end, we discuss the sensitivity of rock mechanical parameters and fracturing parameters at different scales by using dimensionless time parameter τ and dimensionless leak-off parameter ϕ. This paper is organized as follows. First, we introduce the solutions in different propagation regimes based on the dimensionless analysis method. Next, we perform parameter sensitivity analysis at the laboratory and field scales. Subsequently, we conduct experiments simulating the initiation and propagation of hydraulic fractures based on the dimensionless analysis method. Finally, the fracturing parameters under confining stress are analyzed based on the 3D lattice method, which can simulate complex nonplanar fractures.

2. Solutions for a Penny-Shaped Hydraulic Fracture in Different Propagation Regimes

Hydraulic fracturing involves rock deformation, fracture propagation, fluid flow, and leak-off [29]. Therefore, it is a fluid-solid coupling problem with multiscale, nonlinear, and moving boundaries [12]. A variety of hydraulic fracturing theoretical models have been proposed, such as the PKN model, the KGD model, and the penny-shape model [34, 35, 53]. The theoretical solutions are different under different rock mechanical parameters, injection fluid parameters, and boundary conditions. The controlling parameters for the propagation of a penny-shaped hydraulic fracture are determined from scaling laws that recognize the existence of three dissipation processes: dissipation in the fracturing fluid (viscosity), fracturing of the rock (toughness), and fracturing fluid leak-off (leak-off) [12, 53, 54]. The energy dissipated by fracturing fluid flow dominates over the energy consumed by the creation of new fracture surfaces in the viscosity-dominated regime. The opposite holds for the toughness-dominated regime. In the leak-off dominated regime, most of the fracturing fluid leaks into the rock. For instance, in the toughness leak-off regime, leak-off is high, and toughness dominates over viscosity. The solutions are determined by the dimensionless time parameter τ and the dimensionless leak-off ϕ. These limiting fracture propagation regimes based on three energy-dissipating processes can be visualized on a rectangular phase diagram [53], as shown in Figure 1. M and K represent the viscosity-dominated regime and the toughness-dominated regime, respectively. $\tilde{M}$ and $\tilde{K}$ represent the leak-off viscosity-dominated regime and the leak-off toughness-dominated regime, respectively. The transition regime lies in between the limits.

The following material parameters are defined in order to describe the solutions:

$$
\begin{aligned}
\mu' &= 12\mu, \\
E' &= \frac{E}{1-\nu^2}, \\
K' &= 4\left(\frac{2}{\pi}\right)^{1/2} K_{Ic}, \\
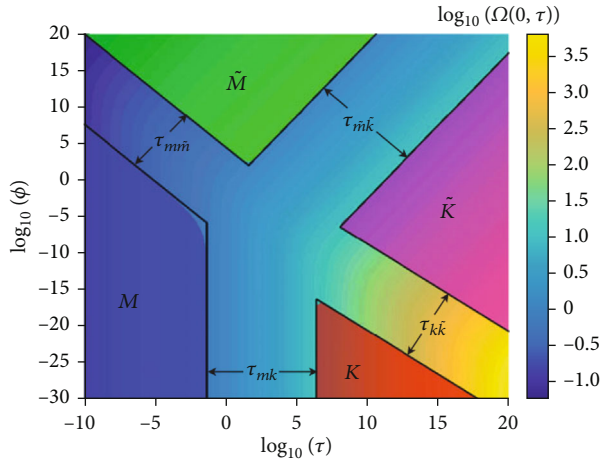C' &= 2C_L.
\end{aligned}
\tag{1}
$$

FIGURE 1: Parametric diagram of limiting fracture propagation regimes versus τ and ϕ for a penny-shaped hydraulic fracture [53].

where E is the modulus of the rock, ν is Poisson's ratio, K_{Ic} is the mode I fracture toughness of the rock, and C_L is the Carter's leak-off coefficient.

For a penny-shaped hydraulic fracture, the dimensionless time τ and the dimensionless leak-off ϕ are defined as [29, 53]

$$\tau = t \left(\frac{\mu'^5 E'^{13} Q_0^3}{K'^{18}} \right)^{-1/2}, \tag{2}$$

$$\phi = \frac{\mu'^3 E'^{11} C'^4 Q_0}{K'^{14}}. \tag{3}$$

Without leak-off, the hydraulic fracture propagates in the toughness-dominated regime if $\tau_{mk} \geq 2.59 \times 10^6$, in the viscosity-dominated regime if $\tau_{mk} \leq 4.54 \times 10^{-2}$, and in the transition regime if $4.54 \times 10^{-2} \leq \tau_{mk} \leq 2.59 \times 10^6$.

When the hydraulic fracture propagates from the viscosity-dominated regime to the leak-off viscosity-dominated regime, the propagation is in the viscosity-dominated regime if $\tau_{m\tilde{m}} \leq 7.41 \times 10^{-6}$, in the leak-off viscosity-dominated regime if $\tau_{m\tilde{m}} \geq 7.2 \times 10^2$, and in the transition regime if $7.41 \times 10^{-6} \leq \tau_{m\tilde{m}} \leq 7.2 \times 10^2$.

When the hydraulic fracture propagates from toughness-dominated regime to leak-off toughness-dominated regime, the propagation is in the toughness-dominated regime if $\tau_{k\bar{k}} \leq 5.96 \times 10^{-8}$, in the leak-off toughness-dominated regime if $\tau_{k\bar{k}} \geq 4.81 \times 10^2$, and in the transition regime if $5.96 \times 10^{-8} \leq \tau_{k\bar{k}} \leq 4.81 \times 10^2$.

When the hydraulic fracture propagates from leak-off viscosity-dominated regime to leak-off toughness-dominated regime, the propagation is in the leak-off viscosity-dominated regime if $\tau_{\tilde{m}\tilde{k}} \leq 4.18$, in the leak-off toughness-dominated regime if $\tau_{\tilde{m}\tilde{k}} \geq 2.01 \times 10^{11}$, and in the transition regime if $4.18 \leq \tau_{\tilde{m}\tilde{k}} \leq 2.01 \times 10^{11}$.

The approximate solution for the viscosity-dominated regime is expressed as [19, 53]

$$w_m(\rho, t) = 1.1901 \left(\frac{\mu'^2 Q_0^3 t}{E'^2} \right)^{1/9} (1 + \rho)^{0.487} (1 - \rho)^{2/3},$$

$$R_m(t) = 0.6944 \left(\frac{Q_0^3 E' t^4}{\mu'} \right)^{1/9}, \tag{4}$$

$$P_m(\rho, t) = 2.4019 \left(\frac{\mu' E'^2}{t} \right)^{1/3} F\left(\rho, 0.487, \frac{2}{3} \right),$$

where R is the fracture radius, $\rho(\rho = r/R)$ is the normalized coordinate along the fracture radius, and r is the distance between the calculation point and the injection point. $F(\rho, \lambda, \chi) = (1/2^{1+\lambda}\pi) \int_0^1 (\partial M(\rho, s)/\partial s)(1 + s)^\lambda (1 - s)^\chi ds$.. $s = R - r$ is the distance from a point inside the fracture to the tip, and χ is a slowly varying function.

$$M(\rho, s) = \begin{cases} \dfrac{1}{\rho} K\left(\dfrac{s^2}{\rho^2} \right) + \dfrac{\rho}{s^2 - \rho^2} E\left(\dfrac{s^2}{\rho^2} \right), & \rho > s, \\[3mm] \dfrac{s}{s^2 - \rho^2} E\left(\dfrac{s^2}{\rho^2} \right), & \rho < s, \end{cases} \tag{5}$$

where functions $K(\cdot)$ and $E(\cdot)$ denote the complete elliptic integrals of the first and the second kind, respectively.

The approximate solution for the leak-off viscosity-dominated regime is expressed as [53, 55]

$$w_{\tilde{m}}(\rho, t) = 1.0574 \left(\frac{\mu'^4 Q_0^6 t}{E'^4 C'^2} \right)^{1/16} (1 + \rho)^{0.397} (1 - \rho)^{5/8}, \tag{6}$$

$$R_{\tilde{m}}(t) = 0.4502 \left(\frac{Q_0^2 t}{C'^2} \right)^{1/4}, \tag{7}$$

$$P_{\tilde{m}}(\rho, t) = 3.0931 \left(\frac{\mu'^4 E'^{12} C'^6}{Q_0^2 t^3} \right)^{1/16} F\left(\rho, 0.397, \frac{5}{8} \right). \tag{8}$$

The approximate solution for the toughness-dominated regime is expressed as [53, 56]

$$w_k(\rho, t) = 0.6537 \left(\frac{K'^4 Q_0 t}{E'^4} \right)^{1/5} (1 - \rho^2)^{1/2},$$

$$R_k(t) = 0.8546 \left(\frac{E' Q_0 t}{K'} \right)^{2/5}, \tag{9}$$

$$P_k(\rho, t) = 0.3004 \left(\frac{K'^6}{E' Q_0 t} \right)^{1/5}.$$

TABLE 1: Sensitivity analysis results of laboratory experimental parameters.

	Modulus/ GPa	Toughness/ MPa·m$^{0.5}$	Carter's leak-off coefficient/m·s$^{-0.5}$	Injection rate (same volume)/ml·min^{-1}	Viscosity/cp	Time/s
Benchmark parameters	30	1.5	6×10^{-5}	120	5	300
Parameters range	10~50	0.5 ~ 3	$1 \times 10^{-5} \sim 2 \times 10^{-4}$	30~1200	0.01~500	30~600
Fracture radius/m	0.32~0.33	0.33~0.32	0.76~0.19	0.23~0.56	0.33~0.32	0.18~0.39
Rangeability of fracture radius	3%	3%	173%	100%	3%	64%
Aperture at injection point/mm	0.18~0.05	0.04~0.12	0.1~0.05	0.05~0.10	0.06~0.14	0.05~0.07
Rangeability of aperture	186%	114%	71%	71%	114%	29%
Pressure at injection point/MPa	2.37~4.08	3.1 ~4.76	1.69~4.22	2.87~3.33	2.33~9.90	4.32~2.56
Rangeability of pressure	60%	70%	88%	16%	264%	61%

The approximate solution for the leak-off toughness-dominated regime is expressed as [53, 57]

$$w_{\tilde{K}}(\rho, t) = 0.4744 \left(\frac{K'^8 Q_0^2 t}{E'^8 C'^2} \right)^{1/8} \left(1 - \rho^2 \right)^{1/2}, \qquad (10)$$

$$R_{\tilde{K}}(t) = 0.4502 \left(\frac{Q_0^2 t}{C'^2} \right)^{1/4}, \qquad (11)$$

$$P_{\tilde{K}}(\rho, t) = 0.4139 \left(\frac{K'^8 C'^2}{Q_0^2 t} \right)^{1/8}. \qquad (12)$$

The approximate solution for the transition regime does not have an explicit expression, see Dontsov [53] for more details.

3. Sensitivity Analysis of Parameters at Different Scales

Parametric design has always been the focus of experiments and has a significant impact on the results of hydraulic fracturing, which can serve as an important reference for field hydraulic fracturing design. Fracturing parameters in experiments differ significantly from field hydraulic fracturing operations. Therefore, we perform sensitivity analysis on rock mechanical parameters and fracturing parameters at different scales by using dimensionless time parameter τ and dimensionless leak-off parameter ϕ. In the sensitivity analysis, only one variable changes at a time, and the other parameters remain the same.

3.1. Sensitivity Analysis of Parameters in Experiments. Table 1 shows the benchmark parameters and parameters ranges in laboratory experiments. According to Equations (2)-(12), the dimensionless time parameter τ and dimensionless leak-off parameter ϕ for benchmark parameters in experiments can be obtained, which are 9.65×10^5 and 6.27×10^{-5}, respectively. The fracture radius, the aperture, and the injection point pressure are 0.33 m, 0.07 mm, and 2.87 MPa, respectively. Therefore, the hydraulic fracture corresponding to the benchmark parameters of the experiment propagates in the transition regime, which is more inclined
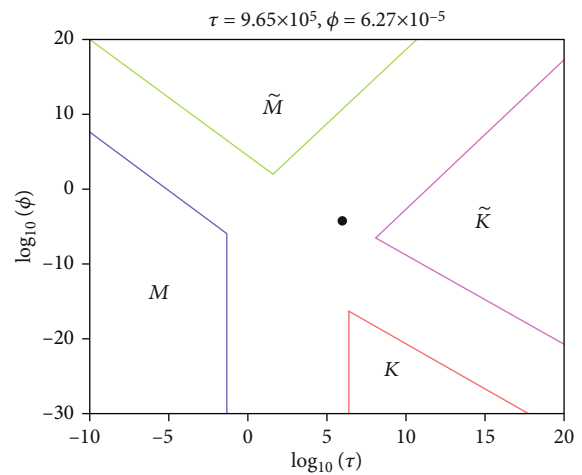

FIGURE 2: Phase diagram location of limiting fracture propagation regimes versus dimensionless time τ and dimensionless leak-off parameter ϕ for benchmark parameters of the experiment [53].

to the leak-off toughness-dominated regime, as shown in Figure 2. The influence of Young's modulus, fracture toughness, Carter's leak-off, injection rate, viscosity, and injection time on fracture radius, aperture, and pressure at the injection point at the experimental scale are listed in Table 1. The rangeability represents the range value divided by the benchmark value.

Figure 3(a) shows the relationship between fracture radius and dimensionless time parameter τ in laboratory experiments, and Figure 3(b) shows the relationship between fracture radius and dimensionless leak-off parameter ϕ. The results show that most of the fracture propagation in the laboratory is in the leak-off toughness-dominated regime, and part is in the leak-off viscosity-dominated regime. As can be seen from Table 1, Carter's leak-off coefficient has the greatest impact on fracture radius, and the range and rangeability of the fracture radius are 0.76~0.19 m and 173%, respectively. According to Equations (2)-(3), Carter's leak-off is related to ϕ, but not to τ. ϕ increases as the Carter's leak-off coefficient increases, so the fracture radius decreases as Carter's leak-off coefficient increases, as shown in Figure 3(b). The second is the effect of injection rate on
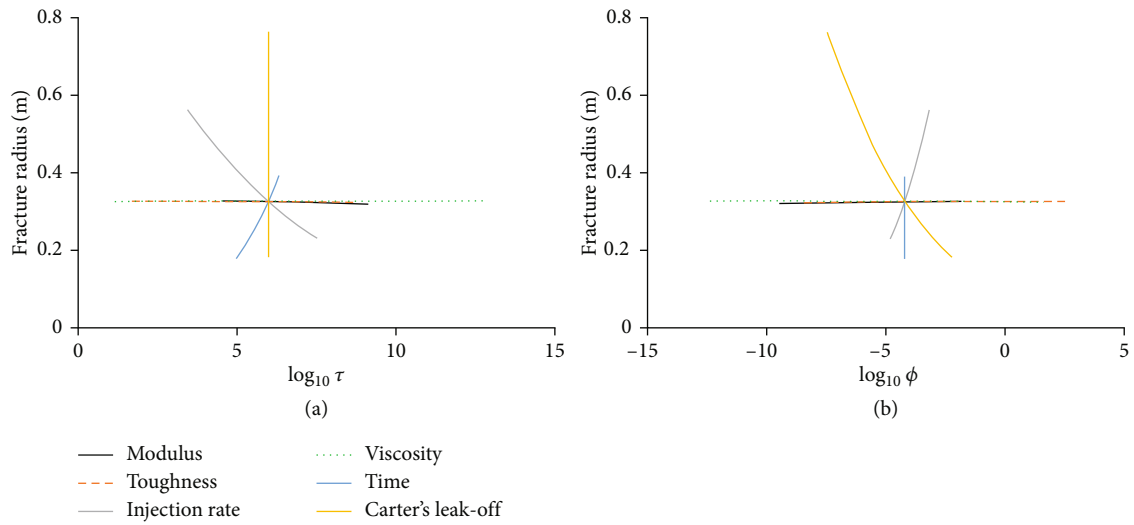
FIGURE 3: Fracture radius versus (a) dimensionless time parameter τ and (b) dimensionless leak-off parameter ϕ in laboratory experiments.
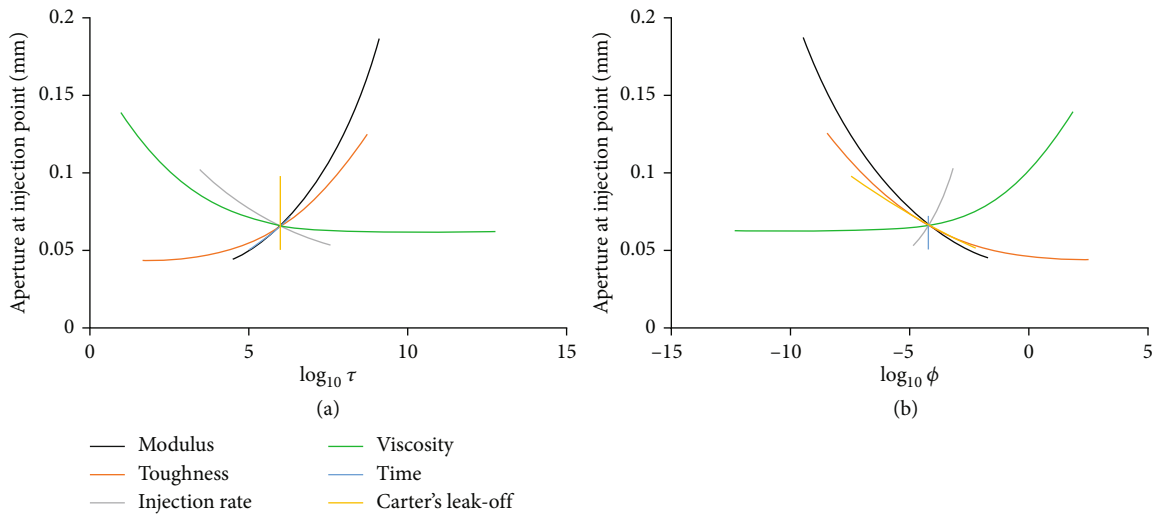

FIGURE 4: Aperture at injection point versus (a) dimensionless time parameter τ and (b) dimensionless leak-off parameter ϕ in laboratory experiments.

fracture radius, and the range and rangeability of the fracture radius are 0.23~0.56 m and 100%, respectively. With the increment of injection rate, τ decreases, while the fracture radius and ϕ increase. Then next is the effect of injection time on fracture radius. The range and rangeability of the fracture radius are 0.18~0.39 m and 64%, respectively. The fracture radius and τ increase over time, and ϕ is independent of time. Therefore, the range of total injected fluid has little impact on energy dissipation, and the energy dissipated by creating new fracture surfaces and leak-off is mainly used for fracture propagation. However, in laboratory experiments, the total injected fluid has a significant impact on fracture radius. Modulus, toughness, and fluid viscosity have little effect on fracture radius, as shown in Figure 3. But the fluid viscosity and toughness have significant impacts on τ and ϕ. The dominant energy dissipation by fracturing fluid viscosity may shift towards the dominant energy dissipation on creating new fracture surfaces as the fluid viscosity changes.

Figure 4(a) displays the relationship between the aperture at injection point and dimensionless time parameter τ in laboratory experiments, and Figure 4(b) displays the relationship between the aperture at injection point and dimensionless leak-off parameter ϕ. The results show that modulus has the greatest influence on aperture. When the rock modulus varies in the range of 10~50 GPa, the range and rangeability of aperture are 0.18~0.04 mm and 186%, respectively. It can be inferred from Equations (2)-(3) that the aperture and τ decrease with increasing modulus. This is followed by the effect of toughness and fluid viscosity on aperture, both of which have a 114% rangeability of aperture. The aperture increases with increasing toughness and fracturing fluid viscosity. When the fracture propagation is in the leak-off toughness-dominated regime, it can be seen from
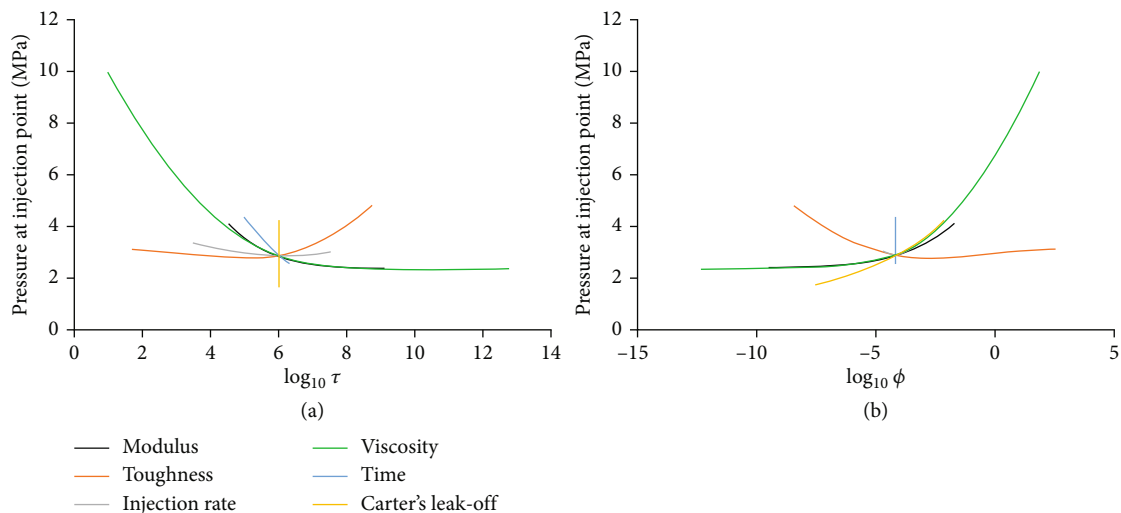
FIGURE 5: Pressure at injection point versus (a) dimensionless time parameter τ and (b) dimensionless leak-off parameter ϕ in laboratory experiments.

TABLE 2: Sensitivity analysis results of field hydraulic fracturing parameters.

	Modulus/ GPa	Toughness/ MPa·m$^{0.5}$	Carter's leak-off coefficient/m·s$^{-0.5}$	Injection rate (same volume)/m^3·min^{-1}	Viscosity/ cp	Time/s
Benchmark parameters	30	1.5	6×10^{-5}	3	5	6000
Parameters range	10~50	0.5~3	$1 \times 10^{-5} \sim 2 \times 10^{-4}$	1~16	0.01~500	1800~10800
Fracture radius/m	100.8~107.4	106.5~104.4	188.2~61.4	84.2~137.0	109.5~93.7	75.2~125.1
Rangeability of fracture radius	6%	2%	119%	50%	15%	47%
Aperture at injection point/mm	3.77~2.05	2.31~2.71	2.76~2.03	1.71~3.78	1.15~7.12	2.15~2.45
Rangeability of aperture	73%	17%	31%	88%	254%	13%
Pressure at injection point/MPa	0.21~0.75	0.51~0.46	0.31~0.77	0.45~0.63	0.13~1.75	0.65~0.45
Rangeability of pressure	108%	10%	92%	36%	324%	40%

Equation (10) that viscosity has no effect on the aperture. Therefore, when the viscosity is smaller than 5cp, the aperture change is small. The influence of injection rate, Carter's leak-off coefficient, and injection time on the fracture aperture ranks the last. Therefore, it is important to pay attention to the influence of rock modulus, fracture toughness, and fracturing fluid viscosity when proppant transport is carried out in hydraulic fracturing experiments.

Figure 5 shows the relationships between injection point pressure and dimensionless time parameter τ and dimensionless leak-off parameter ϕ in laboratory experiments. It can be seen that the fracturing fluid viscosity has the greatest impact on pressure. The range and rangeability of pressure are 2.33~9.90 MPa and 264%, respectively. The pressure increases significantly with the increase of viscosity when the viscosity is greater than 1 cp. However, when the viscosity is less than 1 cp, the fracture propagation mechanism is in the leak-off toughness-dominated regime, and Equation (12) indicates that the pressure in the fracture is independent of viscosity. The second impactful parameter on pressure is the Carter's leak-off, and the range and rangeability of pressure are 1.691~4.221 MPa and 88%, respectively. Equations (8) and (12) indicate that pressure increases with

Carter's leak-off coefficient. The next parameter that has an impact on pressure is toughness. The range and rangeability of pressure are 2.76~4.76 MPa and 70% when the toughness varies in the range of 0.5~3 MPa·m$^{0.5}$. In addition, the fracturing propagation mechanism changes from leak-off viscosity-dominated regime to leak-off toughness-dominated regime. Therefore, when the toughness is less than 1.2 MPa·m$^{0.5}$, the hydraulic fracturing propagation mechanism is close to the leak-off viscosity-dominated regime, and the pressure in the fracture decreases slightly with increasing toughness. When the toughness is greater than 1.2 MPa·m$^{0.5}$, the hydraulic fracturing propagation mechanism is close to the leak-off toughness-dominated regime, and the pressure increases with the toughness, as shown in Figure 5. The last impactful parameter on pressure is the injection time, modulus, and injection rate. Therefore, the effect of fracturing fluid viscosity on pressure should be emphasized in experimental hydraulic fracturing design.

3.2. Sensitivity Analysis of Field Hydraulic Fracturing Parameters. Table 2 lists the benchmark parameters and the parameter ranges for field hydraulic fracturing. The dimensionless time parameter τ and dimensionless leak-off
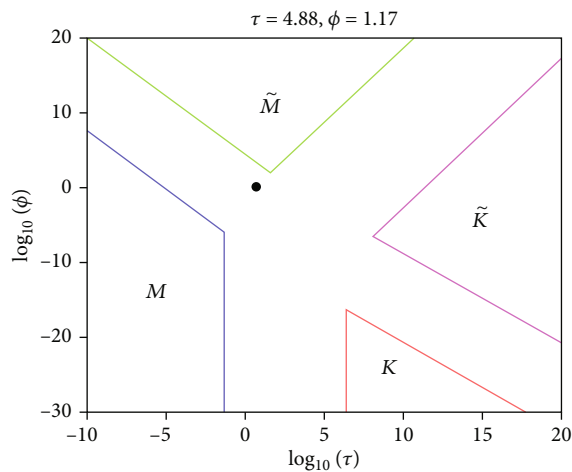
FIGURE 6: Phase diagram location of limiting fracture propagation regimes versus dimensionless time τ and dimensionless leak-off parameter ϕ for field hydraulic fracturing [53].

parameter ϕ for benchmark parameters in field hydraulic fracturing are 4.88 and 1.17, respectively. The fracture radius, aperture and injection point pressure are 106.3 m, 2.35 mm, and 0.5 MPa, respectively. Therefore, field hydraulic fracture corresponding to the benchmark parameters propagates in the transition regime, which is more inclined to the leak-off viscosity-dominated regime, as shown in Figure 6.

Figure 7 shows the relationships between the fracture radius and dimensionless time parameter τ and dimensionless leak-off parameter ϕ in the field hydraulic fracturing. It can be seen that the fracture propagation in the field is mainly in the leak-off viscosity-dominated regime, and part is in the leak-off toughness-dominated regime. Equations (7) and (11) show that fracture radius is mainly related to Carter's leak-off coefficient, injection rate, and injection time, but not related to modulus, toughness, and fluid viscosity. Therefore, the Carter's leak-off coefficient has the greatest impact on the fracture radius, and the fracture radius decreases with increasing Carter's leak-off coefficient. The range and rangeability of fracture radius are 188.2~61.4 m and 119%, respectively. The second parameter that affects fracture radius is the injection rate, and the range and rangeability of fracture radius are 84.2~137.0 m and 50%, respectively. The impact of injection time on fracture radius ranks the next, and the range and rangeability of fracture radius are 75.2~125.1 m and 47%, respectively. In summary, the modulus, toughness, and fluid viscosity have significant impacts on τ and ϕ. Therefore, the sensitivity order of the parameters to fracture radius is the same for field and laboratory hydraulic fracturing.

Figure 8 shows the relationship between aperture at injection point and dimensionless time parameter τ and dimensionless leak-off parameter ϕ in field hydraulic fracturing. Clearly, the fracturing fluid viscosity has the greatest influence on aperture. When the viscosity of the fluid changes in the range of 0.01 to 500 cp, the fracturing propagation changes from leak-off toughness-dominated regime to leak-off viscosity-dominated regime. Fracture aperture

increases with increasing fluid viscosity. The range and rangeability of aperture are 1.15~7.12 mm and 254%, respectively. The second factor affecting the aperture is the injection rate, and the aperture increases with the injection rate. The range and rangeability of the aperture are 3.77~2.05 mm and 73%, respectively. The least impactful parameters influencing aperture are Carter's leak-off coefficient, toughness, and time. In the laboratory experiment, injection rate, fluid viscosity, and toughness have significant effects on fracture width. However, in field hydraulic fracturing, the aperture is mainly affected by the fracturing fluid viscosity, injection rate, and modulus, while toughness has little effect on fracture aperture. Therefore, the sensitivity order of parameters in field hydraulic fracturing is inconsistent with that in laboratory experiments.

Figure 9 shows the relationships between injection point pressure and dimensionless time parameter τ and dimensionless leak-off parameter ϕ in field hydraulic fracturing. Similarly, the fracturing fluid viscosity has the greatest influence on pressure. Specifically, pressure decreases with the decrease of fluid viscosity. The range and rangeability of pressure are 0.13~1.75 MPa and 324%, respectively. The second impactful parameter is the modulus, and the corresponding range and rangeability of pressure are 0.206~0.745 MPa and 108%, respectively. Then there is the effect of Carter's leak-off coefficient on pressure, and the range and rangeability of pressure are 0.313~0.772 MPa and 92%, respectively. Finally, the least impactful parameters are time, injection rate, and modulus. The results of the field hydraulic fracturing show that the pressure range is large, but the pressure range is small. The reason may be that the propagation pressure is stabilized due to prolonged fracturing. Laboratory experiments are limited by sample size and fracturing time, so the propagation pressure is much higher than that of field fracturing.

3.3. Results Analysis. According to the above analyses, the fracturing fluid viscosity has an important effect on hydraulic fracture length, fracture aperture, and pressure in laboratory experiment and has a significant effect on the dimensionless time parameter τ and dimensionless leak-off parameter ϕ. More energy is dissipated by fracturing fluid when the toughness of the sample decreases and the viscosity of the fracturing fluid increases. Therefore, the laboratory tests with small toughness and high fluid viscosity can be used to simulate field hydraulic fracturing (leak-off viscosity-dominated regime). In hydraulic fracturing experiments with proppant transport, the effects of rock modulus, fracture toughness, and fracturing fluid viscosity should be carefully considered. When using low-viscosity fracturing fluid (such as supercritical CO_2) in experiment, the hydraulic fracture propagation is in the leak-off toughness-dominated regime. Therefore, small fracture apertures and uniform fracture pressures can lead to complex hydraulic fractures. Similar results are obtained by numerical simulations and experiments [4, 58, 59].

The energy dissipation during field hydraulic fracturing is mainly consumed by fracturing fluid flow and leak-off. Therefore, the fracture propagation in tight reservoirs is in viscosity-
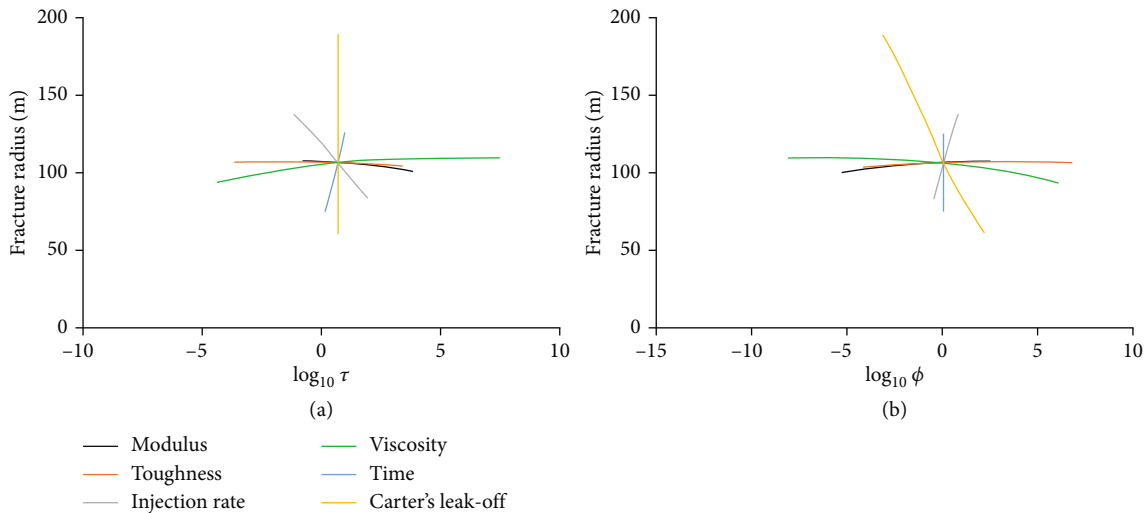
FIGURE 7: Fracture radius versus (a) dimensionless time parameter τ and (b) dimensionless leak-off parameter ϕ for field hydraulic fracturing.
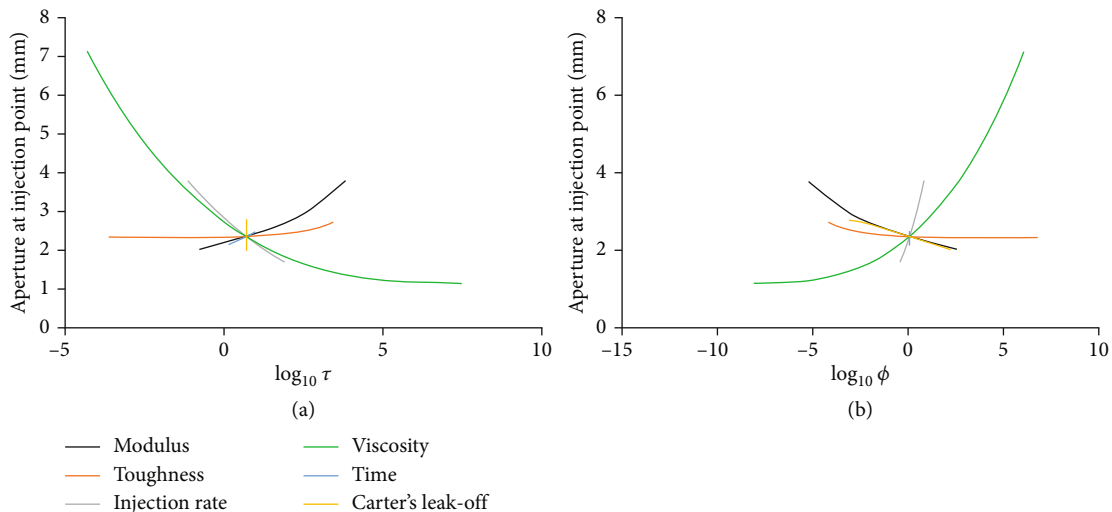

FIGURE 8: Aperture at injection point versus (a) dimensionless time parameter τ and (b) dimensionless leak-off parameter ϕ for field hydraulic fracturing.

dominated regime for small Carter's leak-off coefficient. High-viscosity fracturing fluid can be used in the early stage to create simple hydraulic fractures in the near-wellbore area to reduce twisted fracture geometries and energy dissipation in tight reservoirs. In the later stage, low-viscosity fracturing fluid can be used to create complex hydraulic fracture networks. Most of the fracturing fluid leaks into unconsolidated sandstone reservoirs with high Carter's leak-off coefficient. Therefore, low-viscosity fracturing fluids should be avoided in order to create high-conductivity hydraulic fractures.

4. Physical Testing and Numerical Simulation of Hydraulic Fracturing

4.1. Physical Testing of Hydraulic Fracturing. The above results show that due to the size effect of laboratory experiments, hydraulic fracture propagation is generally in the

transition regime between the toughness-dominated regime and the leak-off toughness-dominated regime, as shown in Figure 2. However, field hydraulic fracture propagation is mainly in the transition regime between viscosity-dominated regime and leak-off viscosity-dominated regime, as shown in Figure 6. Therefore, existing hydraulic fracturing experiments cannot truly simulate the dynamic initiation and propagation of field hydraulic fracturing. After the above parameter analysis, hydraulic fracturing test with high fracturing viscosity is carried out by using a true triaxial hydraulic fracturing apparatus. We monitor the real-time dynamic evolution of hydraulic fractures through acoustic emission to guide the design of field hydraulic fracturing. The dimension of the sample with an open-hole wellbore is 762 mm × 762 mm × 914 mm. The parameters of wellbore and samples are shown in Figure 10. The bottom of the well is sealed with glue to prevent fractures from initiating along
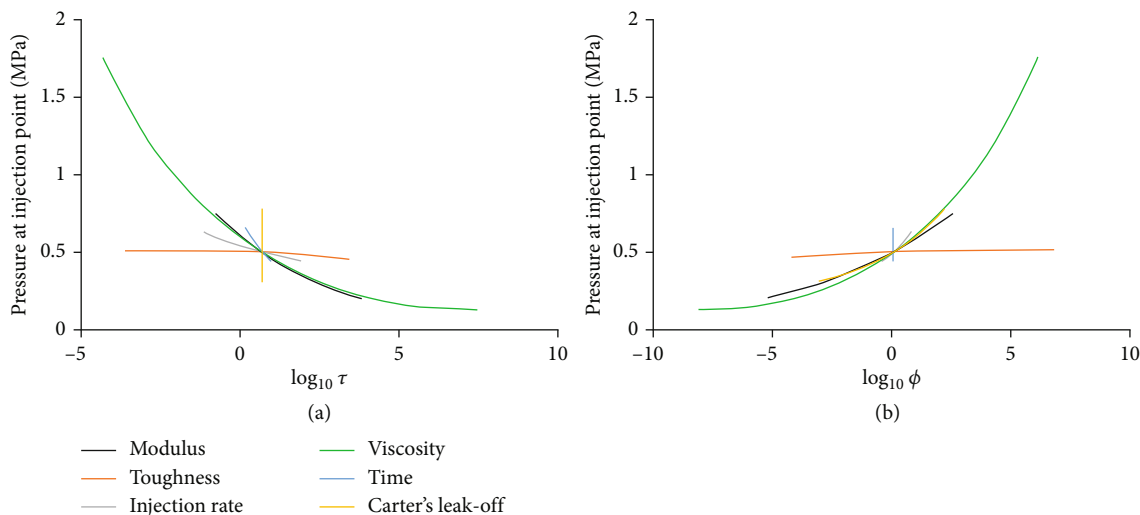
FIGURE 9: Injection point pressure versus (a) dimensionless time parameter τ and (b) dimensionless leak-off parameter ϕ for field hydraulic fracturing.
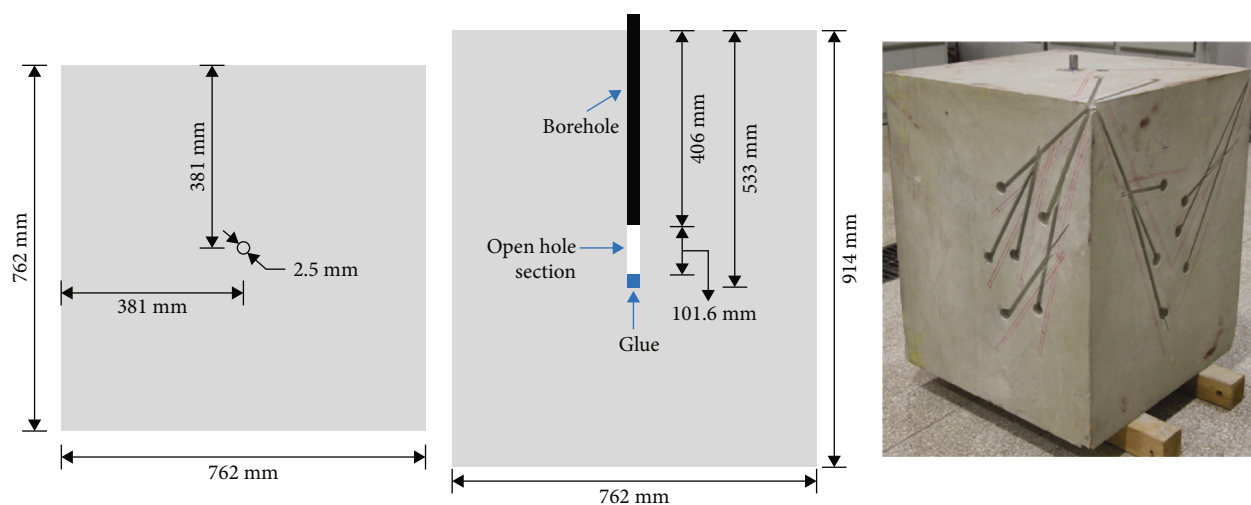

FIGURE 10: Geometries of the wellbore and rock samples.

TABLE 3: Experimental parameters.

Parameters	Modulus/GPa	Toughness/MPa·m$^{0.5}$	Permeability/md	Compressive strength/MPa	Maximum horizontal principal stress/MPa
Value	16	1	0.1	80	14
Parameters	Poisson's ratio	Frictional angle/°	Cohesion/MPa	Tensile strength/MPa	Minimum horizontal principal stress/MPa
Value	0.19	40	6	2	7
Parameters	Density/g·cm^{-3}	Viscosity/mPa·s	Injection rate/ml·min^{-1}	Vertical stress/MPa	
Value	2.7	1000	5~150	21	

the microfractures. The rock mechanical parameters and confining stresses are listed in Table 3. The high viscosity of the fracturing fluid is 1000cp. To observe the fluid leak-off, the initiation, reinitiation, and propagation of fractures, a variable injection rate of 0~150 ml/s is used. When the injection rate is 0.42 ml/s and the injection time is 500 s, the dimensionless time parameters τ is 47.5 and dimensionless leak-off parameters ϕ is 0.0018. The results show

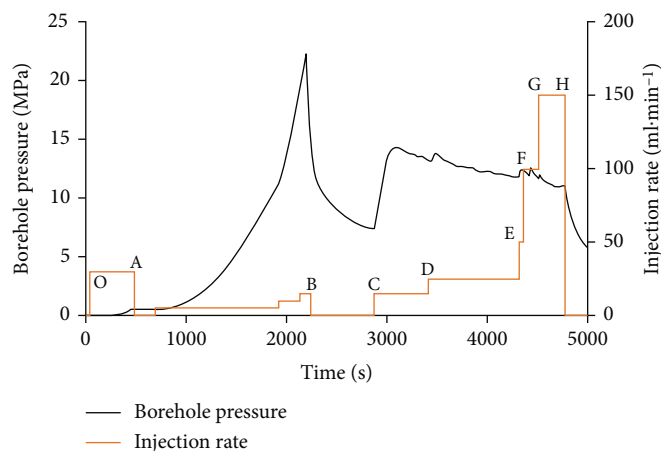FIGURE 11: Borehole pressure history in the laboratory hydraulic fracturing test.

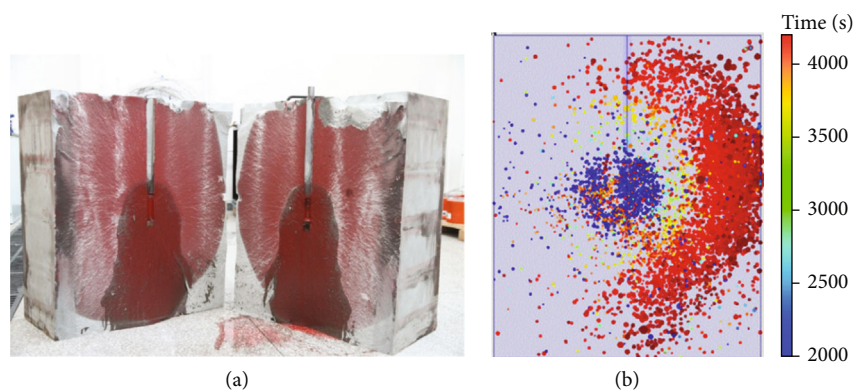(a)   (b)

FIGURE 12: Physical test results, (a) hydraulic fracture geometry, and (b) acoustic emission events.

TABLE 4: Hydraulic fracture radius and borehole pressure at different periods.

Stage	Injection rate/ml·min⁻¹	Injected fluid volume in each period/ml	Hydraulic fracture radius/m	Borehole pressure/MPa
O-A	30	340.37	0	0.52
A-B	0-5-10-15	159.55	0.10	20.31
B-C	0	0.11	0.10	7.38
C-D	15	134.61	0.13	13.21
D-E	25	374.29	0.21	11.77
E-F	50	34.88	0.23	12.28
F-G	100	196.97	0.33	11.66
G-H	150	655.14	0.38	10.96

that the hydraulic fracture propagation is in the transition regime between viscosity-dominated and leak-off viscosity-dominated regimes, which is similar to the field case.

Figure 11 shows the evolution of injection pressure during the experiment. The hydraulic fracture profile and the acoustic monitoring results on the right-side of the sample are shown in Figure 12. In addition, the hydraulic fracture radius and pressure at different times are monitored. The monitoring data are listed in Table 4. On Figure 11, before point O, the confining stress is gradually applied, and the acoustic velocity correction is performed. In the OA period,

the injection begins at 30 ml/min until the injected fluid fills the wellbore. At this point, the wellbore pressure is 0.52 MPa. In the AB period, the injection is stopped. It is observed that the fracturing fluid leak-off is little and the well-bore pressure remains stable. Then we continue to inject at 5 ml/min, and the wellbore pressure increases slowly. The injection rate is then increased to 10 ml/min, and then 15 ml/min and remains stable. The wellbore pressure increases rapidly and reaches the initial breakdown (22.31 MPa), forming an artificial fracture with a radius of 0.1 m. Immediately after the initiation of the fracture, the
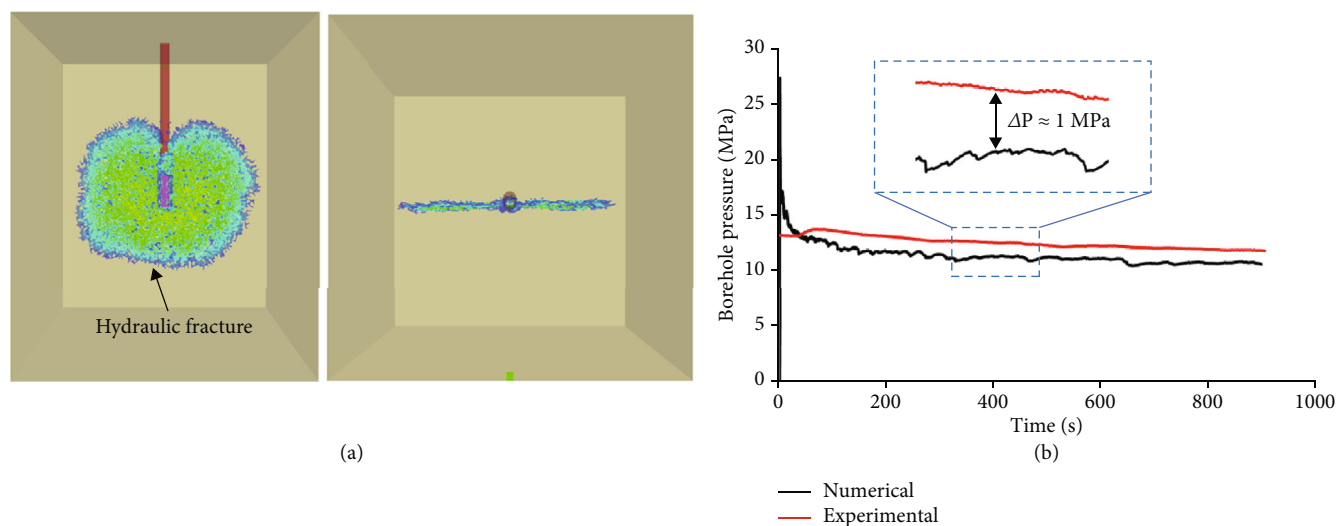
FIGURE 13: (a) Numerical simulation results of the hydraulic fracture and (b) pressure comparison between the numerical simulation and the physical experiment.

pump is stopped. The acoustic monitoring signals are observed in the BC period. The wellbore pressure gradually drops to 7.38 MPa, and the hydraulic fracture does not propagate outward. The fracture initiation is too fast in the early stage, resulting in a fluid lag. After the pump is stopped, the fracturing fluid gradually flows from the front of the fracture to the fracture tip. At the same time, the internal stress of the sample is redistributed, causing defects in the sample to be ruptured and resulting in a small number of acoustic emission events. After point C, we continue to inject again at a rate of 15 ml/min. The breakdown pressure for the refracturing (14.35 MPa) is significantly lower than the initial breakdown pressure (22.31 MPa), and hydraulic fractures slowly extend during the CD period. For the D-E-F-G-H period, the injection rate is gradually increased. The results show that as the injection rate is increased, the wellbore pressure increases slightly during the initial stage but then decreases, indicating that the hydraulic fracture has propagated steadily perpendicular to the direction of the minimum horizontal stress. Finally, a uniform and symmetrical hydraulic fracture is formed.

The dynamic evolution of initiation and propagation of hydraulic fractures is reproduced through laboratory tests. During the initiation of hydraulic fractures, the fluid injected into the hydraulic fractures is less than the injection velocity of the fluid in the wellbore, so the wellbore pressure will continue to increase. When the fluid injected into the fracture is greater than or equal to the fluid injected into the wellbore, the wellbore pressure rises to the fracture pressure. Therefore, the experimental results show that microcracks are created before the injection pressure reaches the breakdown pressure. Deep perforation with large aperture can reduce the initial breakdown pressure. High-viscosity fracturing fluid is recommended to be used in the early stage of fracturing. After a stable primary fracture is generated, the high-viscosity fracturing fluid can be replaced with a low-viscosity fluid to reduce cost.

4.2. Numerical Analysis of Hydraulic Fracturing

4.2.1. Numerical Model Verification. Based on the physical experimental data in Figure 11, we use the 3D lattice method to establish a numerical fracturing model. The 3D lattice method is described in Appendix. In the physical experiment, the fracturing fluid is injected at a variable rate of 15~150 ml/min. In the numerical simulation, a constant injection rate of 25 ml/min in the DE period of the physical experiment is used to simulate hydraulic fracturing. The rock mechanical parameters, confining stresses, and other injection parameters in the numerical model are consistent with the physical experiment, and the Carter's leak-off coefficient is 5.49×10^{-6} m/s$^{1/2}$. Figure 13(a) shows the fracture profile from the numerical model. The hydraulic fracture is symmetrical and radial, which is basically consistent with that of the physical experiment. Figure 13(b) shows a comparison of pressure between the numerical simulation and the physical experiment. The injection rate difference leads to a propagation pressure difference of 1 MPa between the numerical simulation and the experiment, with an error of about 8.5%. Therefore, the results from the numerical model are in good agreement with the experimental results.

4.2.2. Parametric Analysis Using the Numerical Model. The sensitivity analysis of fracturing parameters has been carried out using theoretical solutions; however, the fracturing parameters in the theoretical solutions are solved with zero confining stress. Therefore, in this section, we analyze and study the fracturing parameters under nonzero confining stress condition through the numerical model. We focus on the effects of Carter's leak-off coefficient, injection rate, and confining stress on fracture propagation.

Three different Carter's leak-off coefficients (5.49×10^{-6} m/s$^{1/2}$, 7.62×10^{-6} m/s$^{1/2}$, and 9.14×10^{-6} m/s$^{1/2}$) are selected. Figures 14 and 15 show fracture profiles and pressure data for these three different cases. The larger the
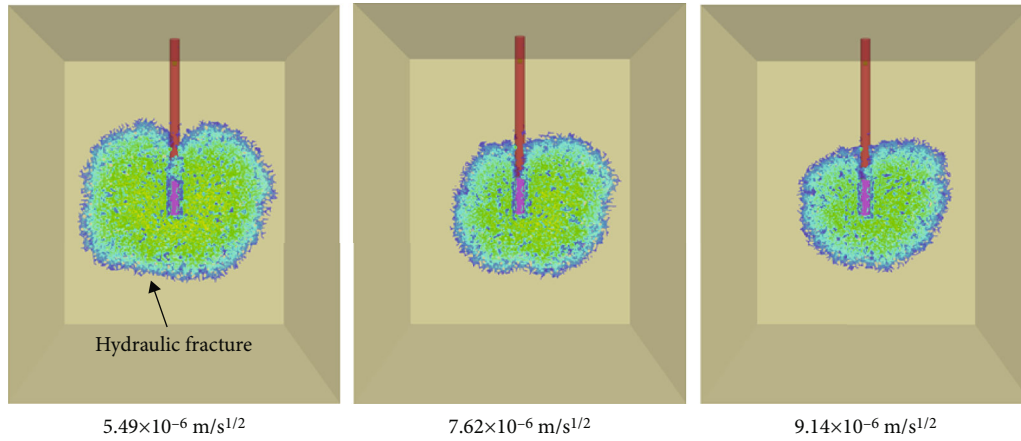
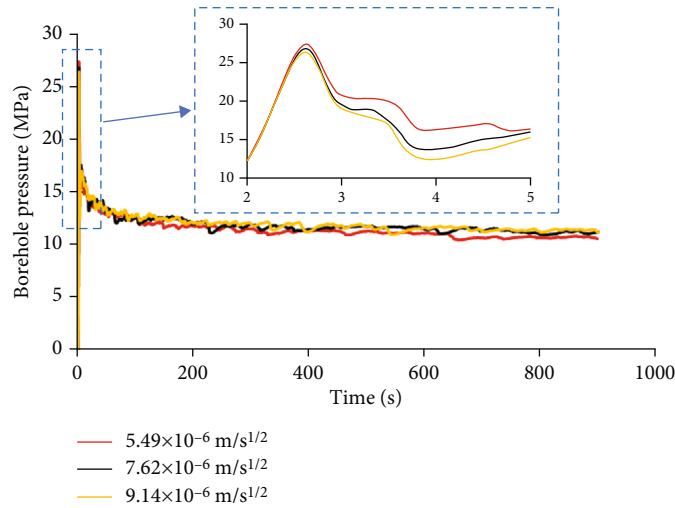FIGURE 14: Hydraulic fracture profiles under different Carter's leak-off coefficients.

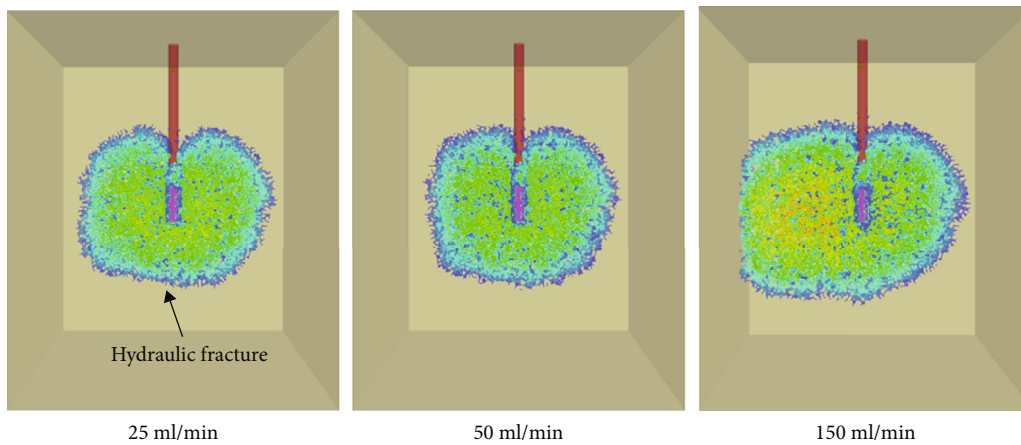FIGURE 15: Pressure history under different Carter's leak-off coefficients.

FIGURE 16: Hydraulic fracture profiles with different injection rates.

Carter's leak-off coefficient, the greater the fluid loss during fracturing, the smaller the nonuniformly asymmetric fracture. During the fracture initiation stage, the fracturing fluid is filtered around the wellbore, reducing the effective stress around the wellbore. But the initiation time is short, so fluid filtration is relatively small. As a result, increasing Carter's
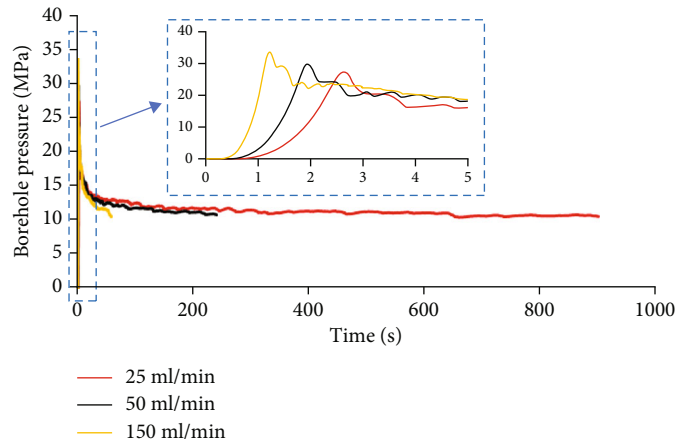
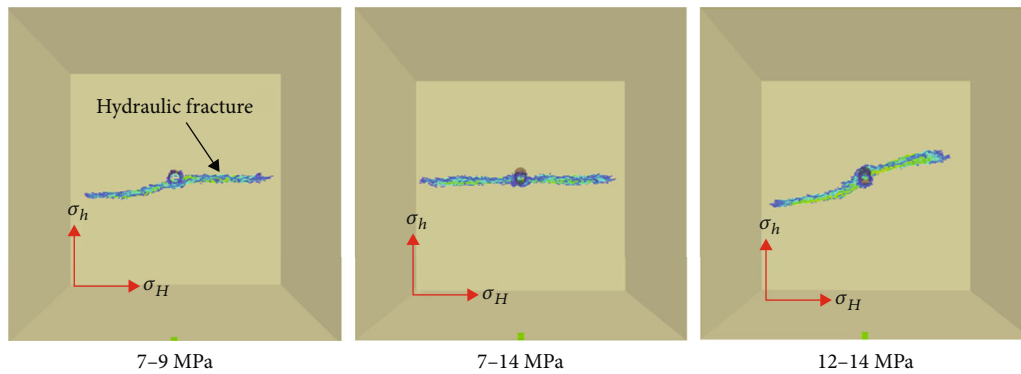FIGURE 17: Borehole pressure histories with different injection rates.

FIGURE 18: Hydraulic fracture profiles with different horizontal principal stress differences.
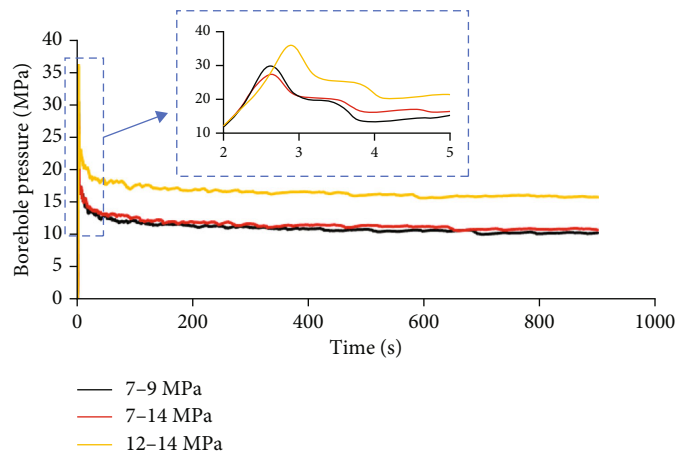

FIGURE 19: Pressure histories with different horizontal principal stress differences.

leak-off coefficient will reduce the breakdown pressure slightly. However, when the hydraulic fracture extends steadily, the propagation pressure increases slightly as Carter's leak-off coefficient increases.

Assuming that the total injected volume is the same, numerical simulations are performed with three injection

rates of 25 ml/min, 50 ml/min, and 150 ml/min. Figures 16 and 17 show the fracture profiles and pressure histories under different injection rates. When the injection rates are 25 ml/min and 50 ml/min, the breakdown pressure are 33.55 MPa and 29.63 MPa, respectively. The hydraulic fractures in these cases are uniform. When the injection rate is

150 ml/min, the hydraulic fracture propagates dominantly to the left. Therefore, when the injection rate is significantly increased, the hydraulic fracture propagates unevenly. As the injection rate increases, the breakdown pressure increases, and the propagation pressure decreases. Therefore, low injection rate is recommended in the initial stage of fracturing in deep or ultradeep reservoirs to reduce the breakdown pressure.

To study the influence of confining stress on fracture propagation, three cases with different stresses (7-9 MPa, 7-14 MPa, and 12-14 MPa) are selected for numerical simulation. Figures 18 and 19 show the fracture profiles and pressures curves with different horizontal principal stresses. We find that the smaller the horizontal principal stress difference, the larger the likelihood a nonplanar asymmetric fracture is created. Under the same horizontal principal stress difference, the larger the minimum principal stress, the more pronounced the asymmetric propagation, and the higher the breakdown pressure and propagation pressure. When the minimum principal stress is the same, the larger the horizontal principal stress difference, the higher the breakdown pressure, but the increase of propagation pressure is relatively small. Therefore, when the principal stress difference is small, the propagation of hydraulic fracture is easily affected by the physical properties of the reservoir, resulting in complex nonplanar fractures. If multiple fractures propagate simultaneously, a complex induced stress field is created, resulting in competitive complex fracture morphologies.

5. Conclusions

In this paper, we conducted parameter sensitivity analysis at laboratory scale and field scale by using the dimensionless analysis method. Based on the results, the initiation and propagation process of the field hydraulic fracturing was reproduced in the laboratory by adjusting the fracturing parameters. Fracturing parameters in the numerical simulation were analyzed under nonzero confining stress condition. The main conclusions of this paper are as follows.

(1) Sensitivity analysis results at different scales show that fracture propagation is affected by many factors. The sensitivity of the fracture propagation velocity, aperture, and pressure distribution in the fracture is different. The fracture propagation in the laboratory is primarily in the leak-off toughness-dominated regime, while the fracture propagation at the field scale is primarily in the leak-off viscosity-dominated regime

(2) The effects of parameters on fracture radius are consistent between the results from the field scale and the laboratory scale, while the effect on fracture aperture and pressure differs. Fluid viscosity has a significant effect on fracture aperture and pressure at different scales. Therefore, the influence of fluid viscosity on hydraulic fracturing should be emphasized in the experimental hydraulic fracturing design
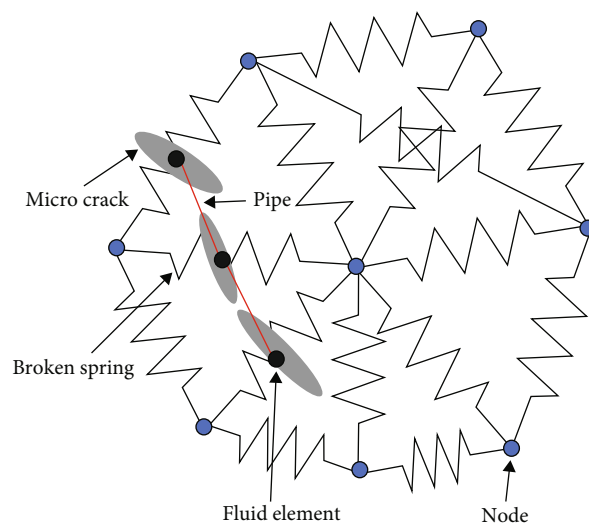

FIGURE 20: Schematic diagram of a 3D discrete lattice model of hydraulic fracturing [15, 23].

(3) The real-time dynamic evolution of hydraulic fractures is characterized by using the acoustic emission technique. The results show that microcracks are generated before breakdown pressure is reached. Numerical simulation results show that Carter's leak-off coefficient has little effect on breakdown pressure and propagation pressure. Injection rate and horizontal principal stress have significant effects on breakdown pressure

Appendix

A. The Three-Dimensional Discrete Lattice Method

The three-dimensional discrete lattice method is a simplified bonded particle model based on the discrete element method [23, 60]. The lattice is composed of a spring connected quasi-random array of three-dimensional nodes with mass, similar to the interconnected structure between particles in the bonded particle model. Springs are equivalent to contacts between particles, and particles are equivalent to mass nodes. Compared to the discrete element model, the discrete lattice method greatly improves the computational efficiency, as shown in Figure 20. Natural fractures can be inserted into the discrete lattice model arbitrarily. Fluid flows in the pipe network between fluid elements. The fluid element is located in the middle of two nodes. The flow channel connecting adjacent fluid elements is called pipe. Multiple connected pipes form a pipe network. Newly created fluid elements at new microfractures are automatically connected to existing fluid elements to generate new pipes while updating the pipe network.

The opening and closing of cracks and joints are highly nonlinear; hence, we use an explicit method to solve the model. Each node consists of three translational degrees of freedom and three angular degrees of freedom. The central

difference formulation of translational degrees of freedom is expressed as

$$\dot{u}_i^{(t+\Delta t/2)} = \dot{u}_i^{(t-\Delta t/2)} + \sum F_i^{(t)} \Delta t/m,$$

$$u_i^{(t+\Delta t)} = u_i^{(t)} + \dot{u}_i^{(t+\Delta t/2)} \Delta t, \qquad (A.1)$$

where $\dot{u}_i^{\,t}$ is the velocity of the component i ($i = 1, 2,$ and 3) at time t, $u_i^{\,t}$ is the displacement of the component i ($i = 1, 2,$ and 3) at time t, $\sum F_i^{(t)}$ is the resultant force of the component i ($i = 1, 2,$ and 3) acting on the node with mass m at time t, and Δt is the time step.

To eliminate the unbalanced moment, the angular degree of freedom needs to be calculated as

$$\omega_i^{(t+\Delta t)} = \omega_i^{(t-\Delta t/2)} + \frac{\sum M_i^{(t)}}{I} \Delta t, \qquad (A.2)$$

where $\sum M_i^{(t)}$ is the resultant moment of the component i ($i = 1, 2,$ and 3) at time t and I is the moment of inertia.

The changes in the spring normal force and tangential force are calculated by the relative displacement of the nodes as

$$F^N \longleftarrow F^N + \dot{u}^N k^N \Delta t,$$

$$F_i^s \longleftarrow F_i^s + \dot{u}_i^s k^s \Delta t, \qquad (A.3)$$

where k^N is the normal stiffness of the spring and k^s is the tangential stiffness.

When F_N exceeds the tensile strength or F_S exceeds the shear strength, the spring breaks. Therefore, there are two failure modes, including tensile failure and shear failure. Microcracks are generated after the breakage of the spring. At this point, $F_N = 0$ and $F_S = 0$.

Prefabricated fractures and newly generated fractures are connected by pipes in the fluid network. The classical lubrication equation is used to describe the fluid flow in the pipe. The flow rate from fluid node A to node B is written as

$$q = \beta k_r \frac{a^3}{12\mu} \left[p^A - p^B + \rho_w g \left(z^A - z^B \right) \right], \qquad (A.4)$$

where β is a dimensionless correction parameter, k_r is the relative permeability, which is a function related to saturation, p_A and p_B are the pressures at nodes A and B, respectively, z_A and z_B are the heights at nodes A and B, respectively, ρ_w is the fluid density, and g is the acceleration of gravity.

The explicit numerical method is used to solve the flow model. The pressure increment ΔP with a fluid time step Δt_f is calculated as

$$\Delta P = \frac{Q}{V} \bar{K}_F \Delta t_f, \qquad (A.5)$$

where $\bar{K}_F$ is the fluid modulus, V is the fluid volume at the node, and Q is the sum of all flow rates in the pipes connected to the node.

Data Availability

All the data and materials that support the findings used in this paper are available from the corresponding author upon reasonable request.

Conflicts of Interest

The authors declare that they have no conflicts of interest.

Acknowledgments

References

[1] L. Huang, J. Liu, Y. Ji, X. Gong, and L. Qin, "A review of multi-scale expansion of low permeability reservoir cracks," *Petroleum*, vol. 4, no. 2, pp. 115–125, 2018.

[2] B. Kong, E. Fathi, and S. Ameri, "Coupled 3-D numerical simulation of proppant distribution and hydraulic fracturing performance optimization in Marcellus shale reservoirs," *International Journal of Coal Geology*, vol. 147-148, pp. 35–45, 2015.

[3] B. Lecampion, A. Bunger, and X. Zhang, "Numerical methods for hydraulic fracture propagation: a review of recent trends," *Journal of Natural Gas Science and Engineering*, vol. 49, pp. 66–83, 2018.

[4] M. Li, F. Zhang, L. Zhuang, X. Zhang, and P. Ranjith, "Micromechanical analysis of hydraulic fracturing in the toughness-dominated regime: implications to supercritical carbon dioxide fracturing," *Computational Geosciences*, vol. 24, no. 5, pp. 1815–1831, 2020.

[5] N. P. Roussel and M. M. Sharma, "Quantifying transient effects in altered-stress refracturing of vertical wells," *SPE Journal*, vol. 15, no. 3, pp. 770–782, 2010.

[6] H. Shimizu, S. Murata, and T. Ishida, "The distinct element analysis for hydraulic fracturing in hard rock considering fluid viscosity and particle size distribution," *International Journal of Rock Mechanics and Mining Sciences*, vol. 48, no. 5, pp. 712–727, 2011.

[7] J. Tang, K. Wu, L. Zuo, L. Xiao, S. Sun, and C. Ehlig-Economides, "Investigation of rupture and slip mechanisms of hydraulic fractures in multiple-layered formations," *SPE Journal*, vol. 24, no. 5, pp. 2292–2307, 2019.

[8] P. L. P. Wasantha, H. Konietzky, and C. Xu, "Effect of in-situ stress contrast on fracture containment during single- and multi-stage hydraulic fracturing," *Engineering Fracture Mechanics*, vol. 205, pp. 175–189, 2019.

[9] L. P. Yi, H. Waisman, Z. Z. Yang, and X. G. Li, "A consistent phase field model for hydraulic fracture propagation in

poroelastic media," *Computer Methods in Applied Mechanics and Engineering*, vol. 372, article 113396, 2020.

[10] F. Zhang, L. Huang, L. Yang et al., "Numerical investigation on the effect of depletion-induced stress reorientation on infill well hydraulic fracture propagation," *Petroleum Science*, vol. 19, no. 1, pp. 296–308, 2022.

[11] X. Zhang, R. G. Jeffrey, and M. Thiercelin, "Deflection and propagation of fluid-driven fractures at frictional bedding interfaces: a numerical investigation," *Journal of Structural Geology*, vol. 29, no. 3, pp. 396–410, 2007.

[12] E. Detournay, "Mechanics of hydraulic fractures," *Annual Review of Fluid Mechanics*, vol. 48, no. 1, pp. 311–339, 2016.

[13] E. V. Dontsov, "An approximate solution for a plane strain hydraulic fracture that accounts for fracture toughness, fluid viscosity, and leak-off," *International Journal of Fracture*, vol. 205, no. 2, pp. 221–237, 2017.

[14] F. Zhang, B. Damjanac, and S. Maxwell, "Investigating hydraulic fracturing complexity in naturally fractured rock masses using fully coupled multiscale numerical modeling," *Rock Mechanics and Rock Engineering*, vol. 52, no. 12, pp. 5137–5160, 2019.

[15] L. Huang, J. Liu, F. Zhang, H. Fu, H. Zhu, and B. Damjanac, "3D lattice modeling of hydraulic fracture initiation and near-wellbore propagation for different perforation models," *Journal of Petroleum Science and Engineering*, vol. 191, article 107169, 2020.

[16] Z. Yin, H. Huang, F. Zhang, L. Zhang, and M. Shawn, "Three dimensional distinct element modeling of fault reactivation and induced seismicity due to hydraulic fracturing injection and flowback," *Journal of Rock Mechanics and Geotechnical Engineering*, vol. 12, no. 4, pp. 752–767, 2020.

[17] Y. Zeng, X. Zhang, and Z. Baoping, "Stress redistribution in multi-stage hydraulic fracturing of horizontal wells in shales," *Petroleum Science*, vol. 12, no. 4, pp. 628–635, 2015.

[18] X. Zhang, R. G. Jeffrey, and M. Thiercelin, "Escape of fluid-driven fractures from frictional bedding interfaces: a numerical study," *Journal of Structural Geology*, vol. 30, no. 4, pp. 478–490, 2008.

[19] Y. Zheng, R. He, L. Huang et al., "Exploring the effect of engineering parameters on the penetration of hydraulic fractures through bedding planes in different propagation regimes," *Computers and Geotechnics*, vol. 146, article 104736, 2022.

[20] X. Zhuang, S. Zhou, M. Sheng, and G. Li, "On the hydraulic fracturing in naturally-layered porous media using the phase field method," *Engineering Geology*, vol. 266, article 105306, 2020.

[21] Y. Zou, X. Ma, T. Zhou et al., "Hydraulic fracture growth in a layered formation based on fracturing experiments and discrete element modeling," *Rock Mechanics and Rock Engineering*, vol. 50, no. 9, pp. 2381–2395, 2017.

[22] H. Fatahi, M. M. Hossain, and M. Sarmadivaleh, "Numerical and experimental investigation of the interaction of natural and propagated hydraulic fracture," *Journal of Natural Gas Science and Engineering*, vol. 37, pp. 409–424, 2017.

[23] B. Damjanac and P. Cundall, "Application of distinct element methods to simulation of hydraulic fracturing in naturally fractured reservoirs," *Computers and Geotechnics*, vol. 71, pp. 283–294, 2016.

[24] Z. P. Bažant, M. Salviato, V. T. Chau, H. Visnawathan, and A. Zubelewicz, "Why fracking works," *Journal of Applied Mechanics*, vol. 81, no. 10, 2014.

[25] X. Weng, "Modeling of complex hydraulic fractures in naturally fractured formation," *Journal of Unconventional Oil and Gas Resources*, vol. 9, pp. 114–135, 2015.

[26] M. J. Altammar, S. Agrawal, and M. M. Sharma, "Effect of geological layer properties on hydraulic-fracture initiation and propagation: an experimental study," *SPE Journal*, vol. 24, no. 2, pp. 757–794, 2019.

[27] H. M. An, H. Y. Liu, H. Han, X. Zheng, and X. G. Wang, "Hybrid finite-discrete element modelling of dynamic fracture and resultant fragment casting and muck-piling by rock blast," *Computers and Geotechnics*, vol. 81, pp. 322–345, 2017.

[28] E. Detournay, "Propagation regimes of fluid-driven fractures in impermeable rocks," *International Journal of Geomechanics*, vol. 4, no. 1, pp. 35–45, 2004.

[29] E. V. Dontsov and F. Zhang, "Calibration of tensile strength to model fracture toughness with distinct element method," *International Journal of Solids and Structures*, vol. 144-145, pp. 180–191, 2018.

[30] D. I. Garagash, "Cohesive-zone effects in hydraulic fracture propagation," *Journal of the Mechanics and Physics of Solids*, vol. 133, article 103727, 2019.

[31] R. G. Jeffrey and A. Bunger, "A detailed comparison of experimental and numerical data on hydraulic fracture height growth through stress contrasts," *SPE Journal*, vol. 14, no. 3, pp. 413–422, 2009.

[32] Z. Liu, Z. Pan, S. Li et al., "Study on the effect of cemented natural fractures on hydraulic fracture propagation in volcanic reservoirs," *Energy*, vol. 241, article 122845, 2022.

[33] F. E. Moukhtari, B. Lecampion, and H. Zia, "Planar hydraulic fracture growth perpendicular to the isotropy plane in a transversely isotropic material," *Journal of the Mechanics and Physics of Solids*, vol. 137, article 103878, 2020.

[34] S. A. Khristianovic and Y. P. Zheltov, "Formation of Vertical Fractures by Means of Highly Viscous Liquid," in *4th World Petroleum Congress*, Rome, Italy, 1955.

[35] T. K. Perkins and L. R. Kern, "Widths of hydraulic fractures," *Journal of Petroleum Technology*, vol. 13, no. 9, pp. 937–949, 1961.

[36] N. B. Nagel, M. A. Sanchez-Nagel, F. Zhang, X. Garcia, and B. Lee, "Coupled numerical evaluations of the geomechanical interactions between a hydraulic fracture stimulation and a natural fracture system in shale formations," *Rock Mechanics and Rock Engineering*, vol. 46, no. 3, pp. 581–609, 2013.

[37] A. D. Taleghani, "Analysis of hydraulic fracture propagation in fractured reservoirs: an improved model for the interaction between induced and natural fractures: the University of Texas at Austinhttps://repositories.lib.utexas.edu/bitstream/handle/2152/18381/dahitaleghania23003.pdf?sequence=2.

[38] X. Tang, J. Rutqvist, M. Hu, and N. M. Rayudu, "Modeling three-dimensional fluid-driven propagation of multiple fractures using TOUGH-FEMM," *Rock Mechanics and Rock Engineering*, vol. 52, no. 2, pp. 611–627, 2019.

[39] H. Tang, S. Wang, R. Zhang, S. Li, L. Zhang, and Y. S. Wu, "Analysis of stress interference among multiple hydraulic fractures using a fully three-dimensional displacement discontinuity method," *Journal of Petroleum Science and Engineering*, vol. 179, pp. 378–393, 2019.

[40] X.-d. Ni, Y. Wang, K. Chen, and S.-l. Zhao, "Improved similarity criterion for seepage erosion using mesoscopic coupled PFC–CFD model," *Journal of Central South University*, vol. 22, no. 8, pp. 3069–3078, 2015.

[41] A. Peirce and E. Detournay, "An implicit level set method for modeling hydraulically driven fractures," *Computer Methods in Applied Mechanics and Engineering*, vol. 197, no. 33-40, pp. 2858–2885, 2008.

[42] L. Huang, E. Dontsov, H. Fu, Y. Lei, D. Weng, and F. Zhang, "Hydraulic fracture height growth in layered rocks: perspective from DEM simulation of different propagation regimes," *International Journal of Solids and Structures*, vol. 238, article 111395, 2022.

[43] F. Zhang, E. Dontsov, and M. Mack, "Fully coupled simulation of a hydraulic fracture interacting with natural fractures with a hybrid discrete-continuum method," *International Journal for Numerical and Analytical Methods in Geomechanics*, vol. 41, no. 13, pp. 1430–1452, 2017.

[44] G. Basson, A. P. Bassom, and B. Salmon, "Simulating hydraulic fracturing preconditioning in mines with the material point method," *Journal of Applied Geophysics*, vol. 195, article 104471, 2021.

[45] M. Qin, D. Yang, W. Chen, and S. Yang, "Hydraulic fracturing model of a layered rock mass based on peridynamics," *Engineering Fracture Mechanics*, vol. 258, article 108088, 2021.

[46] C. Yan and H. Zheng, "A two-dimensional coupled hydro-mechanical finite-discrete model considering porous media flow for simulating hydraulic fracturing," *International Journal of Rock Mechanics and Mining Sciences*, vol. 88, pp. 115–128, 2016.

[47] S. Zhou, X. Zhuang, and T. Rabczuk, "Phase-field modeling of fluid-driven dynamic cracking in porous media," *Computer Methods in Applied Mechanics and Engineering*, vol. 350, pp. 169–198, 2019.

[48] L. Huang, J. Liu, F. Zhang, E. Dontsov, and B. Damjanac, "Exploring the influence of rock inherent heterogeneity and grain size on hydraulic fracturing using discrete element modeling," *International Journal of Solids and Structures*, vol. 176-177, pp. 207–220, 2019.

[49] W. Zhao, G. Ji, K. Li, W. Liu, L. Xiong, and J. Xiao, "A new pseudo 3D hydraulic fracture propagation model for sandstone reservoirs considering fracture penetrating height," *Engineering Fracture Mechanics*, vol. 264, article 108358, 2022.

[50] P. Liu, Y. Ju, P. G. Ranjith, Z. Zheng, and J. Chen, "Experimental investigation of the effects of heterogeneity and geostress difference on the 3D growth and distribution of hydrofracturing cracks in unconventional reservoir rocks," *Journal of Natural Gas Science and Engineering*, vol. 35, pp. 541–554, 2016.

[51] P. Tan, H. Pang, R. Zhang et al., "Experimental investigation into hydraulic fracture geometry and proppant migration characteristics for southeastern Sichuan deep shale reservoirs," *Journal of Petroleum Science and Engineering*, vol. 184, article 106517, 2020.

[52] X. Weng and E. Siebrits, "Effect of Production-Induced Stress Field on Refracture Propagation and Pressure Response," in *SPE Hydraulic Fracturing Technology Conference*, pp. 1–9, College Station, Texas, USA, 2007.

[53] E. V. Dontsov, "An approximate solution for a penny-shaped hydraulic fracture that accounts for fracture toughness, fluid viscosity and leak-off," *Royal Society Open Science*, vol. 3, no. 12, 2016.

[54] E. Detournay and D. I. Garagash, "The near-tip region of a fluid-driven fracture propagating in a permeable elastic solid," *Journal of Fluid Mechanics*, vol. 494, pp. 1–32, 2003.

[55] E. A. Kanin, E. V. Dontsov, D. I. Garagash, and A. A. Osiptsov, "A radial hydraulic fracture driven by a Herschel–Bulkley fluid," *Journal of Non-Newtonian Fluid Mechanics*, vol. 295, article 104620, 2021.

[56] E. V. Dontsov, "Morphology of multiple constant height hydraulic fractures versus propagation regime," *International Journal for Numerical and Analytical Methods in Geomechanics*, vol. 46, no. 6, pp. 1177–1183, 2022.

[57] E. V. Dontsov, "An efficient computation of leak-off induced poroelastic stress for a hydraulic fracture," *Journal of the Mechanics and Physics of Solids*, vol. 147, article 104246, 2021.

[58] B. Deng, G. Yin, M. Li et al., "Feature of fractures induced by hydrofracturing treatment using water and L-CO_2 as fracturing fluids in laboratory experiments," *Fuel*, vol. 226, pp. 35–46, 2018.

[59] B. Deng, G. Yin, D. Zhang, M. Li, Y. Liu, and J. Lu, "Experimental investigation of fracture propagation induced by carbon dioxide and water in coal seam reservoirs," *Powder Technology*, vol. 338, pp. 847–856, 2018.

[60] D. Potyondy and P. A. Cundall, "A bonded-particle model for rock," *International Journal of Rock Mechanics and Mining Sciences*, vol. 41, no. 8, pp. 1329–1364, 2004.